Material Properties of Ceramic Slurries for Applications in Additive Manufacturing Using Stereolithography

Erin Maines[1], Nelson Bell[1], Lindsey Evans[1], Matthew Roach[1], Lok-kun Tsui[2], Judith Lavin[1], David Keicher[3]

[1]Sandia National Laboratories, Albuquerque NM, 87185
[2]Center for MicroEngineered Materials, University of New Mexico, Albuquerque NM, 87106
[3]Integrated Deposition Solutions, Albuquerque NM, 87110

Abstract

Stereolithography (SL) is a process that uses photosensitive polymer solutions to create 3D parts in a layer by layer approach. Sandia National Labs is interested in using SL for the printing of ceramic loaded resins, namely alumina, that we are formulating here at the labs. One of the most important aspects for SL printing of ceramics is the properties of the slurry itself. The work presented here will focus on the use of a novel commercially available low viscosity resin provided by Colorado Photopolymer Solutions, CPS 2030, and a Hypermer KD1 dispersant from Croda. Two types of a commercially available alumina powder, Almatis A16 SG and Almatis A15 SG, are compared to determine the effects that the size and the distribution of the powder have on the loading of the solution using rheology. The choice of a low viscosity resin allows for a high particle loading, which is necessary for the printing of high density parts using a commercial SL printer. The Krieger-Dougherty equation was used to evaluate the maximum particle loading for the system. This study found that a bimodal distribution of micron sized powder (A15 SG) reduced the shear thickening effects caused by hydroclusters, and allows for the highest alumina powder loading. A final sintered density of 90% of the theoretical density of alumina was achieved based on the optimized formulation and printing conditions.

1. Introduction

Stereolithography (SL) is an Additive Manufacturing (AM) form of 3D printing using a UV light source to print photopolymerizable solutions in a layer-by-layer method. SL is attractive for manufacturing intricate ceramic parts because it allows for detail and precision that is not available with conventional methods, such as a standard press mold or extrusion (Hinczewski, 1998). The focus of this paper is on ceramic, specifically alumina, highly loaded photopolymerizable slurries for creating ceramic parts that are hard to make with traditional molding methods. SL can be used to create ceramic green parts in a layer-by-layer method by exposing a slurry containing a ceramic powder and a photopolymerizable monomer solution to light in a specific pattern (Johansson, 2017). Typical light sources used to initiate polymerization are masks using Digital Light Processing (DLP) technology or laser sources (Halloran, 2016; Hinczewski, 1998). This paper focuses on the use of a commercially available digital light projector from Digital Light Innovations run with a Kudo 3D control system (Kudo/DLP).

After the green part is created using the SL printer, it goes through a debinding/burnout and sintering process to achieve the final density. Current research has focused on creating high density alumina parts that have densities comparable to traditional ceramics. Recent studies have shown that theoretical densities above 99.3% can be achieved using SL technology (Schwentenwein, 2015). To achieve high density parts the alumina material should have a greater than 40 vol% loading in the photopolymerizable monomer solution, or resin (Li, 2016). The rheological behavior of the final slurry itself is very important for a successful print. Typical SL slurries have a shear thinning behavior and viscosities around 3 Pa s at 30 s^{-1} (Li, 2016). The viscosities for the slurries used in this paper were evaluated using a HAAKE MARS II Rheometer. The rheometer allows for a measurement of the viscosity of the slurry, the yield stress, and an evaluation of the slurry behavior at different shear rates.

The focus in this study is on commercially available low viscosity resins to achieve highly loaded alumina slurries that can successfully print using SL technology to achieve densities greater than 90% theoretical density and have low shrinkage. The low viscosity resin is used to compare two different particle types: a bimodal particle distribution with peak around 0.5 µm and 5 µm, and a unimodal particle distribution around 0.5 µm. Wu et al. have shown that mixing both nano- and micro-sized alumina powder for SL slurries could achieve better final sintered densities (Wu, 2016). This study focuses on micron sized particle distributions to determine their effect on the rheology of the slurry.

2. Materials and Methods

2.1 Materials

The alumina powder used in this study was Almatis A15 SG, a commercially available alumina powder with a $d_{50} = 1.7$ µm and an average surface area of 4.9 m^2/g. Almatis A15 SG was tested against a smaller powder, Almatis A16 SG with a $d_{50} = 0.5$ µm and an average surface area of 8.9 m^2/g (Alumina, n.d.). A typical particle size distribution curve for these materials is shown below in Fig. 1. To identify the optional formulation, several dispersants were experimented with and Hypermer KD1 was identified as the optimal dispersant for this resin system. Hypermer KD1 has been shown to create successful dispersion of alumina particles in a paper by Johansson (2017). The main low viscosity resin used in this system was provided by Colorado Photopolymer Solutions (CPS) called CPS 2030.
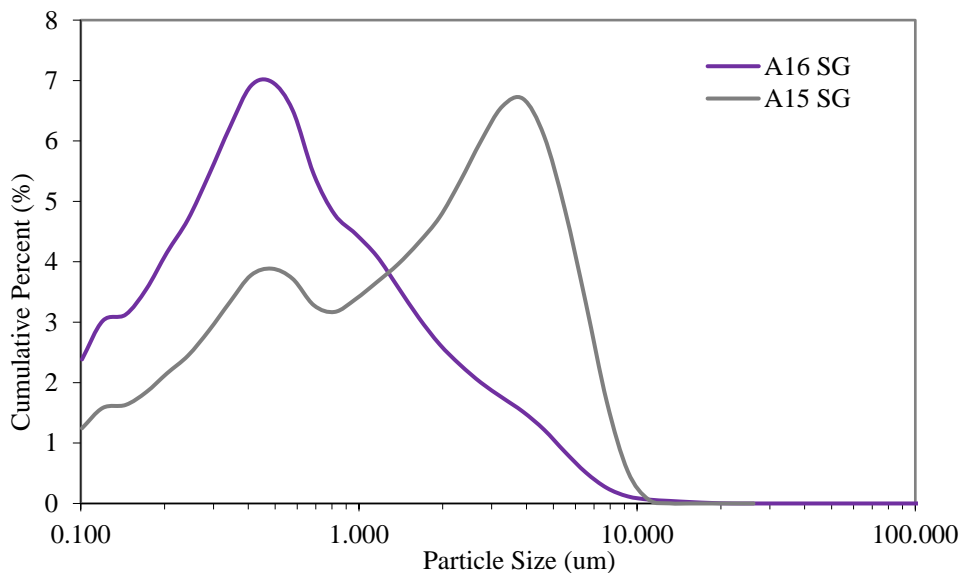
Figure 1. Typical particle size distribution curve for A15 SG and A16 SG (C. Compson, personal communication, May 9, 2018).

Three versions of CPS 2030 were provided with different photoinitiator systems using the same resin base. The neat viscosity for the CPS 2030 system is approximately 0.026 Pas at 25°C at a shear rate of $10s^{-1}$. The three different versions of CPS 2030 were created to be sensitive at different wavelengths using different photoinitiator systems as shown in Table 1 below. Photoinitiator A has low sensitivity to 405 nm light with the main peak centering just above 300nm. At 0.1wt%, A is highly sensitive at 365nm with a short tail at 400nm; therefore, this photoinitiator is optimal for use on the Kudo/DLP printer. Photoinitiator B at 0.1wt% has a peak at 365nm and therefore is optimal for use with both the 365nm light source and the 405nm light source. Lastly, C is a sensitizer with an absorbance peak at 365nm added with the photoinitiator A to improve absorption at 405nm. The work presented here pertains to the first version of CPS 2030, because it has a low base viscosity, as shown in Table 1 below, and successfully prints on the Kudo/DLP system.

Table 1. Three different resin types with the associated photoinitiator and viscosity.

Resin Version	Photoinitiator	Viscosity at $10s^{-1}$ (Pa s)
CPS 2030	A	0.026 ± 0.0008
CPS 2030 V.2	B	0.023 ± 0.0003
CPS 2030 V.3	A, C	0.031 ± 0.0005

2.2 Methods

Before the slurries could be prepared, the alumina powder was ball milled with 5mm YSZ beads with 1wt% of the KD1 dispersant in Toluene for 24 hours. The powder was set out to dry, and then crushed and sieved through a number 40 sieve. The powder/dispersant mixture and the resin were then mixed varying from 10-65vol% of alumina powder in the resin using a planetary centrifugal mixer (Thinky) to ensure adequate mixing. To determine the optimal concentration of dispersant, a 10wt% stock solution of KD1 in CPS 2030 was prepared and used to create various concentrations of KD1 in CPS 2030 with 50vol% A15 alumina powder. The viscosities of all slurries were evaluated using a HAAKE MARS II Rheometer with a 35mm 1°Ti cone and plate by varying the shear rate from $0.1s^{-1}$ to $1000s^{-1}$.

After the slurry was prepared, the part of varying size and complexity were printed on the Kudo/DLP system to create green parts. In this case, the focus of the paper is on ceramic cylinders with heights of 4.5mm and an outer diameter of 7.5mm. The green parts then underwent the burnout and sintering process. The shrinkage of the parts was determined using a VHX Digital Microscope, and the density was determined using the Archimedes test in DI water. X-ray tomography was taken of the parts using an Industrial Microfocus CT system from North Star Imaging to determine inter- and intra-layer cracking. The specific settings used with the Microfocus CT scan are included in Table 2 below. Thermogravimetric analysis (TGA) was also run on each of the individual components of the slurry, as well as the slurry as a whole, to determine the burnout profile using a TGA/DSC 1 from Mettler Toledo.

Table 2. Microfocus CT Scan Settings

System Hardware and Software	
Shielded Cabinet	Steel-lead-steel construction
X-ray Source	FeinFocus FXE-225, 10kV to 225kV
Flat-panel Detector	Premium Grade CsI 1621 Perkin Elmer (40cm x 40cm)
Software	NSI efX-DR, efX-CT, Volume Graphics VG Studio MAX
Scan Parameters	
Voltage	150kV
Current	55 µÅ
Pixel Pitch	200 x 200 µm
Frame Rate	2 fps
Number of projections	1371
Frames Averaged	6
System Magnification	23.96x
Tube to detector distance	749.135mm
Tube to part distance	31.264mm
Effective pixel size	8.3 µm
Pre-filter	0.6mm Cu, 3.2mm Al

3. Results

3.1 Dispersant Loading and Resin Choice

CPS 2030 was used to determine the optimal dispersant loading for this system at a 50vol% A15 loading. A 50vol% loading was chosen to allow the material to flow freely to get a more accurate measurement of the viscosity using the rheometer. The dispersant loading was varied every 0.5wt% between 0.5wt% and 2wt%. Fig. 2 below, shows the lowest viscosity was recorded at 1wt% KD1 in CPS 2030; therefore, this dispersant loading was chosen for creating slurries for SL printing.
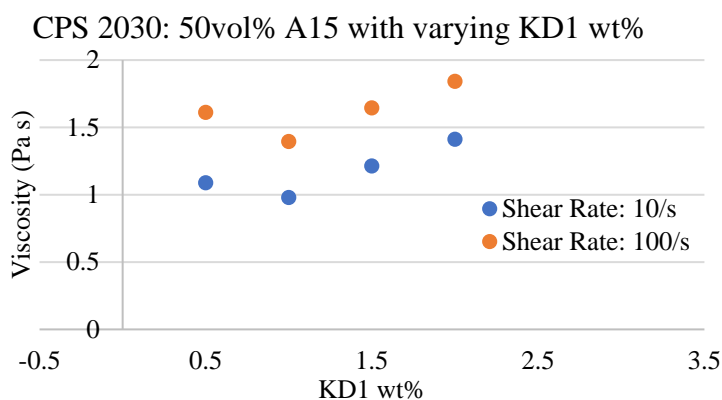
Figure 2. 50vol% A15 with varying amounts of KD1 in CPS 2030.

3.2. A15 SG vs A16 SG Powder

A16 SG powder was considered as a method to potentially increase density in the final sintered part because the smaller powder size would reduce the possibility of voids being created during sintering. A15 powder was prepared at 55.1vol% A15 with 1wt% KD1 in CPS 2030. The A16 powder was prepared at 43.9vol% A16 with 1wt% KD1 in CPS 2030, and 55vol% A16 with 2wt% KD1 in CPS 2030. Fig. 3 below shows the average values for each sample at shear rates of 10 s^{-1}. Two mixtures of A16 were created because it was suspected that there was not enough dispersant at 1wt% to cover the higher surface area per gram of the A16 particles, as indicated by the high viscosity at a much lower particle loading of the A16 (43.9vol% A16 with 1wt% KD1), as compared to the A15 (1wt% KD1) sample. The large error associated with the 43.9vol% A16 is due to the first few runs of the sample having a viscosity greater than 100 Pas at 10s^{-1}. Increasing the amount of KD1 in the A16 system decreased the viscosity significantly, to allow for higher loading with a lower viscosity.
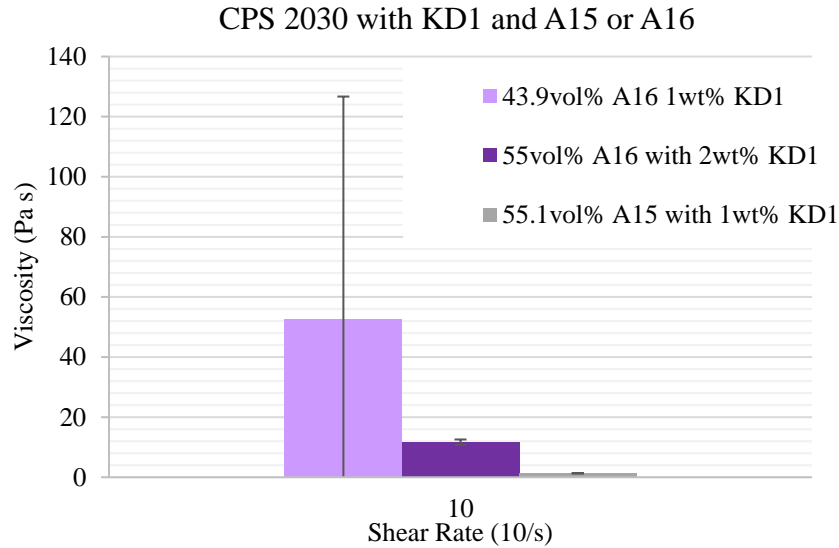
Figure 3. Viscosity of CPS 2030 with 55.1vol% A15 and 1wt% KD1 (gray), CPS 2030 with 43.9vol% A16 and 1wt% KD1 (light purple), and CPS 2030 with 55vol% A16 and 2wt% KD1 (dark purple).

The proper loading of A15 and A16 was then determined by varying the A15 or A16 amount within the CPS 2030 resin/KD1 dispersant system. For both systems, as the loading increased, the shear thickening behavior also increased as shown in Fig. 4 and Fig. 5 below. The shear thickening behavior became more pronounced and occurred at lower shear rates with an increase in particle loading. This sudden increase in viscosity at lower shear rates with an increase in particle loading is described with shear thickening as a function of the formation of hydroclusters (Mewis, 2012). Hydroclusters are defined as local transient fluctuations in particle density and are present in systems with reversible shear thickening behavior (Mewis, 2012). For true shear thickening behavior, the shear stress at the onset of shear thickening should stay the same with increasing loading; however, for this system the shear stress also increases slightly as shown in Fig. 6 and Fig. 7, due to the dispersant on the surface of the particles potentially altering the hydrodynamic flow that creates the hydroclusters (Mewis, 2012).
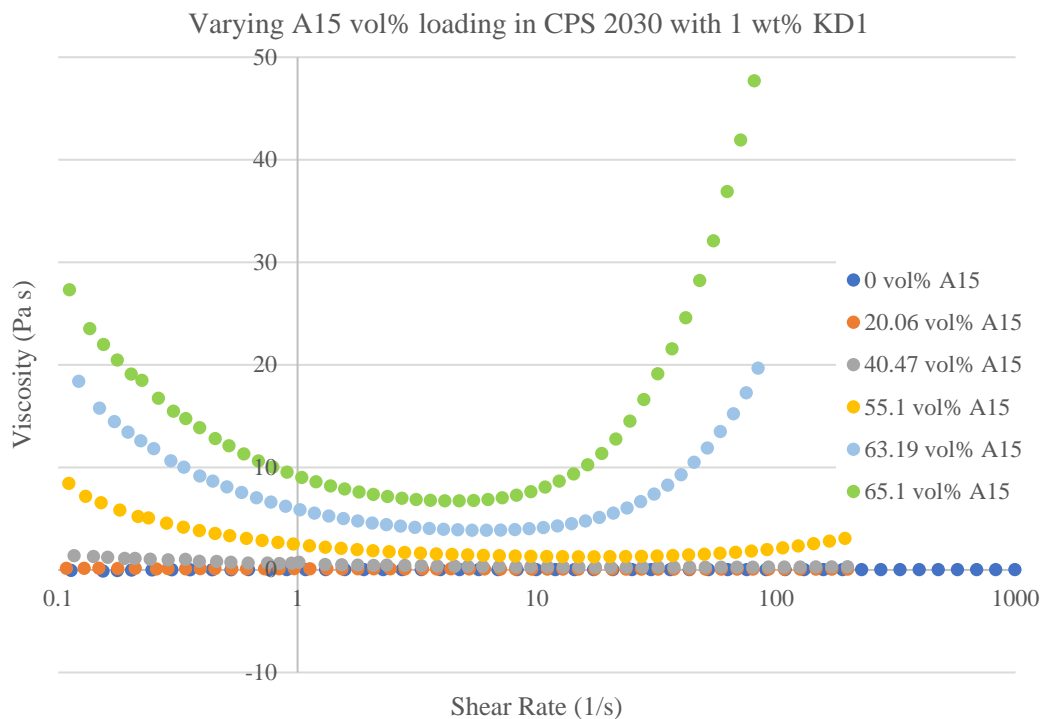
Figure 4. Varying A15 volume percent with a constant 1wt% of KD1 in CPS 2030. Data shown is a representative sample of all the viscosity runs.
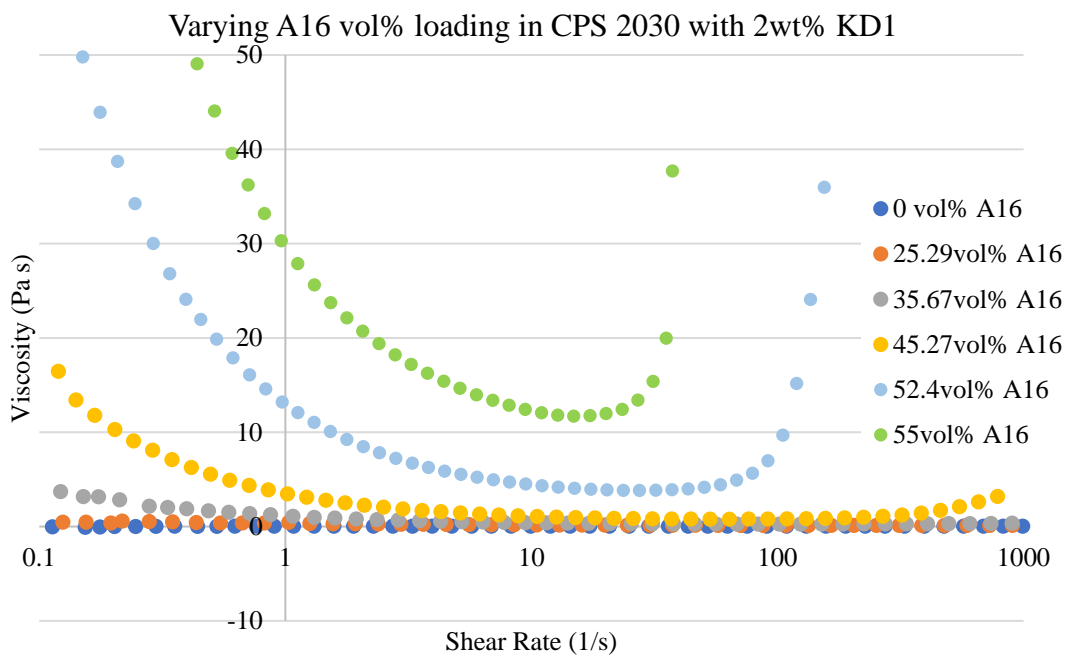

Figure 5. Varying A16 volume percent with a constant 2wt% of KD1 in CPS 2030. Data shown is a representative sample of all the viscosity runs.
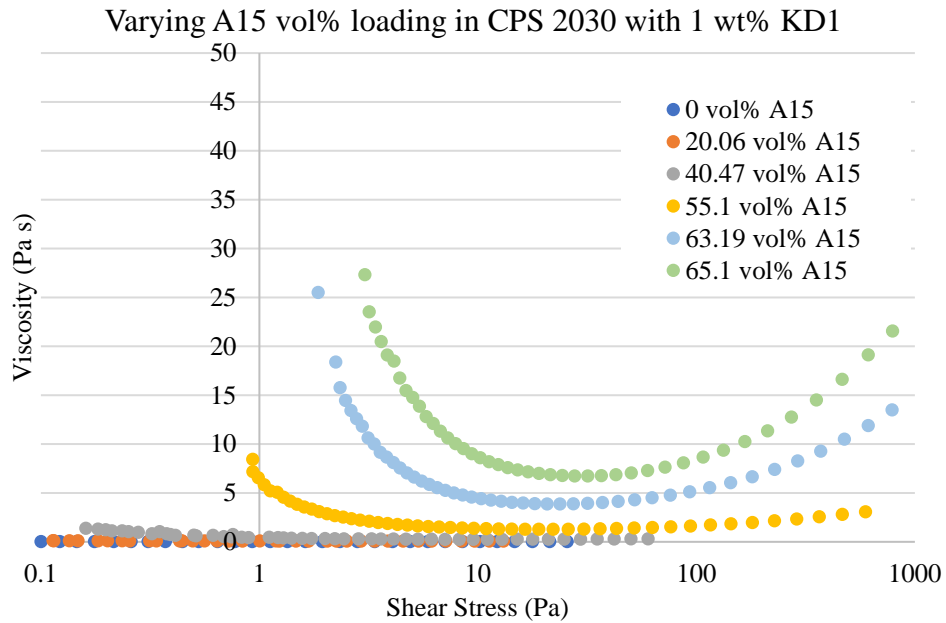
Figure 6. Varying A15 volume percent with a constant 1wt% of KD1 in CPS 2030. Data shown is a representative sample of all the viscosity runs.
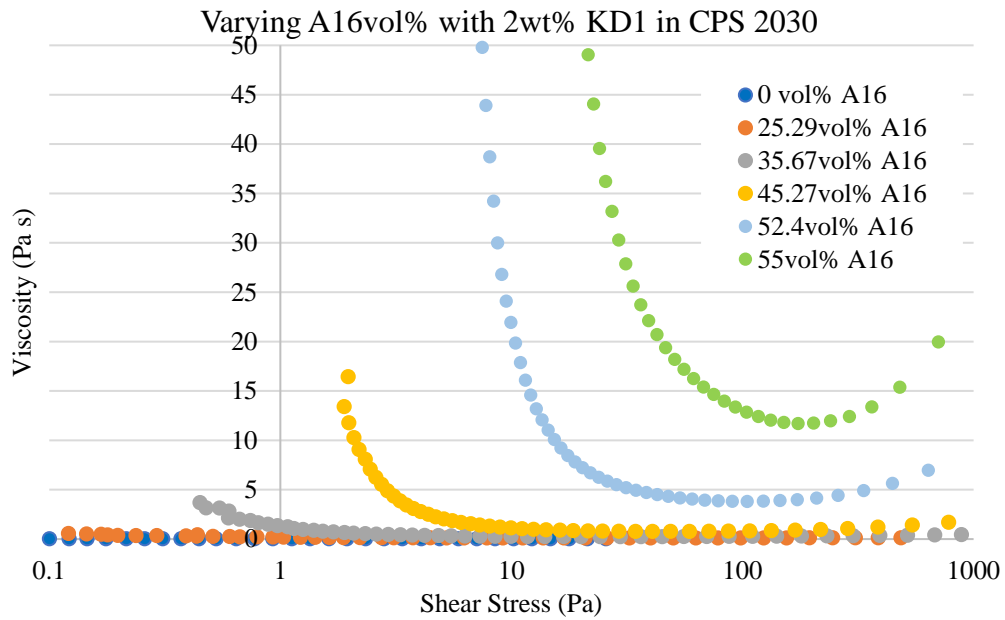

Figure 7. Varying A16 volume percent with a constant 2wt% of KD1 in CPS 2030. Data shown is a representative sample of all the viscosity runs.

The viscosity as a function of the volume percent loading of the A15 and A16 powder was then isolated at a low shear rate of 10s^{-1} and graphed as shown in Fig. 8 below. The Krieger-Dougherty equation is valid for low shear rates, so 10s^{-1} was chosen as the lowest shear rate that allowed for a valid measurement. Varying the volume percent loading allows for a determination of the maximum loading for this resin using the Krieger-Dougherty equation as shown in Eqn. 1 below.

$$n_r = (1 - \frac{\phi}{\phi_m})^{-[n]\phi_m} \tag{1}$$

where n_r is the viscosity measured divided by the reference fluid viscosity (in this case 0 vol% alumina loading in CPS 2030), ϕ is the fraction loaded, ϕ_m is the maximum loading, and $[n]$ is a shape factor or the intrinsic viscosity indicating the shape of the particles in solution (Hunter, 1989). Fitting the Krieger-Dougherty equation to the A15 data, the maximum loading was 76 vol% A15 and the shape factor was 3.88. The A16 data fit to the Krieger-Dougherty equation yielded a maximum loading of 61vol% and a shape factor of 4.34. A typical shape factor for a perfect sphere is 2.5, and a perfect cube is 4, so a shape factor of 3.88 is consistent with a particle with imperfect edges between a cube and a sphere, and a shape factor of 4.34 is consistent with an imperfect cube. A maximum loading of 71% is expected for perfect identical spheres with hexagonal close packing or face-centered cubic packing (Hiemenz, 1997). A maximum loading above 71% could be possible because of the size distribution of the A15 particles. A15 has a mixture of small and large particles so the smaller particles could fill in the gaps to create a slightly higher maximum packing. A16 creates a lower packing density than A15 indicating that the bimodal distribution of particle sizes is very important to create highly loaded SL slurries. The A16 slurries also have a consistantly higher viscosity than the A15 slurries preventing highly loaded slurries that maintain a viscosity below 5 Pas to allow for it to be printed on a SL printer. Due to the posibility of higher particle loadings with A15, as well as the lower viscosities associated with A15 particles, A15 particles were pursued for use in the SL system.
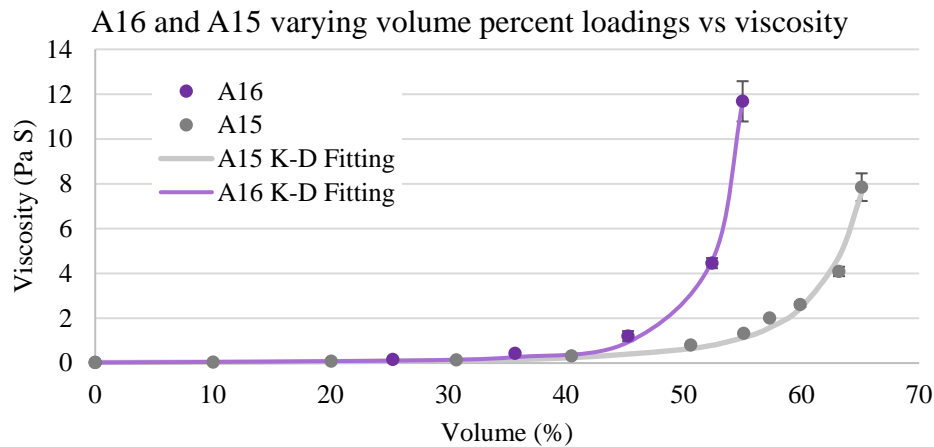

Figure 8. Varying Alumina A15 vol% with 1wt% KD1 in CPS 2030. Varying Alumina A16 vol% with 2wt% KD1 in CPS 2030. Average data evaluated at a shear rate of 10s^{-1}. Solid lines show the Krieger-Dougherty Equation fit.

3.3 Final Parts

Parts using 55.5vol% A15 with 1wt% KD1 in CPS 2030 were successfully printed using the Kudo/DLP printer system and sent through the burnout and sintering process. Data for shrinkage and density were obtained from 4 samples. Of the 4 samples that were printed, 2 of the samples were polished using 600 and 180 grit sandpaper prior to burnout and sintering. The difference in the surface before and after polishing can be seen below in Fig. 9. The unpolished surface is on the left and the polished surface is on the right. The support features on the left were removed during the polish and some of the bumps have been smoothed away from the surface.
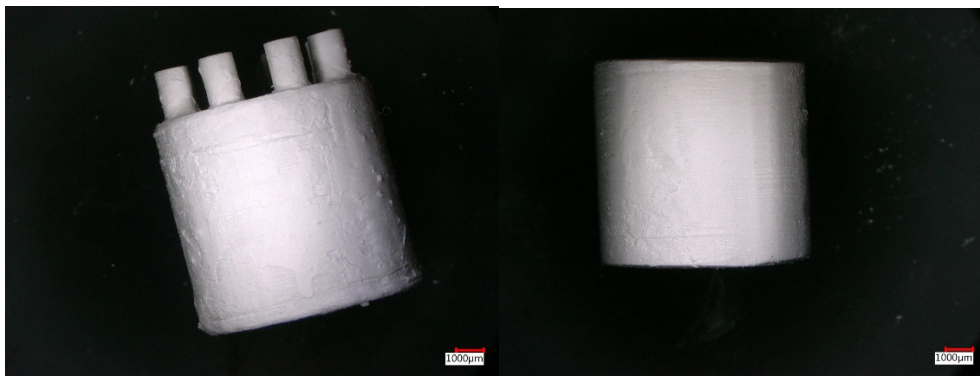

Figure 9. Side images using a VHX Digital Microscope. Part #1 Unpolished (left), Polished (Right).

The shrinkage of the parts is shown below in Table 3. The average volume shrinkage was about 34% ± 5%. The shrinkage was higher in the height, or z-direction, with slightly less shrinkage in the x,y direction as indicated by the outer diameter shrinkage. A comparison of part #1 before and after sintering is shown below in Fig. 10. The surface looks similar, but the edges are slightly more rounded on the sintered part due to the shrinkage during the sintering step.

Table 3. 55.5vol% A15 with 1wt% KD1 in CPS 2030 part shrinkage after burnout and sintering.

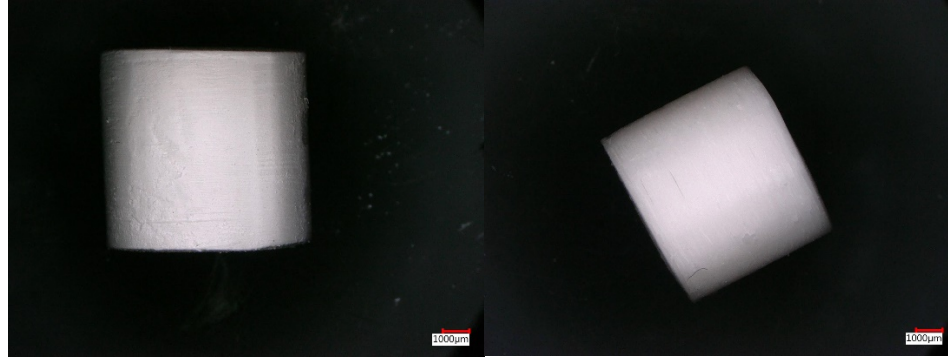| Part Identification	Height Shrinkage	Outer Diameter Shrinkage	Volume Shrinkage
1. Polished	16%	14%	40%
2. Polished	14%	10%	32%
3. Unpolished	14%	11%	29%
4. Unpolished	17%	12%	35%
Average	15% ± 2%	12% ± 2%	34% ± 5%

Figure 10. Side images using a VHX Digital Microscope. Part #1 Green Part (Left), Sintered Part (Right).

The final density of the parts was evaluated using the Archimedes method in DI water. The final densities are shown in Table 4 below as a percent of the theoretical density of alumina. The two polished parts achieved over 90% theoretical density, meeting our requirements for this project. The unpolished samples reached over 88% theoretical density. Smith et al in 1984 showed that a particle distribution of this type (5µm and 0.5 µm) could reach around 90% theoretical density, as was observed in this experiment (Smith, 1984). Further testing is required to determine the extent polishing has on the final sintered densities; however, all the samples are similar in density within the standard deviation.

Table 4. Percent of Theoretical Density for Kudo/DLP system.

Part Identification	Density
1. Polished	91.8%
2. Polished	90.5%
3. Unpolished	89.3%
4. Unpolished	88.7%
Average	90% ± 1.4%

X-ray tomography through two of the samples (#1 and #3) were taken to determine the extent of the cracking and the formation of cracks inside the samples. Cracking is common with the burnout and sintering of ceramics parts created with binder. Only one of the two samples are shown below because the profile between the two samples is very similar. Fig. 11 shows the cracking from the top down on the left, and the cracking from the side on the right. The top down view shows that there is some cracking within the layers themselves; however, most of the cracking is between the layers as shown in the photo on the right in Fig. 11. When looking at the side view, the middle of the sample walls contains some interlayer cracking, but a lot of the crack propagation is along the layer boundaries. These cracks open to the surface would also affect the Archimedes density measured and contribute to the lowered density observed in this experiment. The interlayer cracking could be a function of the burnout and sintering program, and could be tuned to further reduce this cracking.
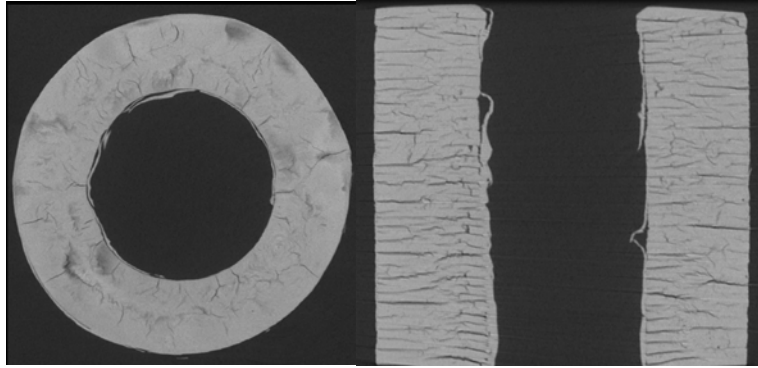
Figure 11. X-ray tomography for the 55.5vol% A15 with 1 wt% KD1 in CPS 2030 sintered cylinder from Kudo/DLP system.

To try to identify some of the causes of cracking, TGA was run on the plain CPS 2030 resin, the Alumina (A15) with 1wt% KD1, and the resin that was printed on the Kudo/DLP system (55.5vol% A15 with 1wt% KD1 in CPS 2030) to determine how the different materials burn off during the burnout step. From Fig. 12 below, the red line indicating the plain resin shows that the resin does not fully burn off, but leaves about 10% of material behind, but most of the material burns around 375°C and ends around 450°C. This peak is also seen in full slurry sample (black line), indicating the start of the resin burn off in the SL slurry is not changed in the solution. The blue line in Fig. 12 shows a steep increase right at start up for the alumina with KD1, then an initial decrease, and then increase in material to 108% once the material reaches 1000°C. The initial decrease could be due to the KD1 burning off, and the increase in material weight could be an indication of oxidation of the material, a decrease in density of the surrounding air with heat, or due to the sensitivity of the instrument scale (Mettler Toledo, n.d.). This increase is also reflected in the SL slurry burn off. The other large drop in the slurry from 150°C to 250°C can be contributed to an earlier, smaller burnout of some resin material. The TGA data could be useful to further tune the burnout process to eliminate cracks by slowing the temperature ramp during the burnout of the resin, between 150°C to 250°C, and 350°C to 450°C.
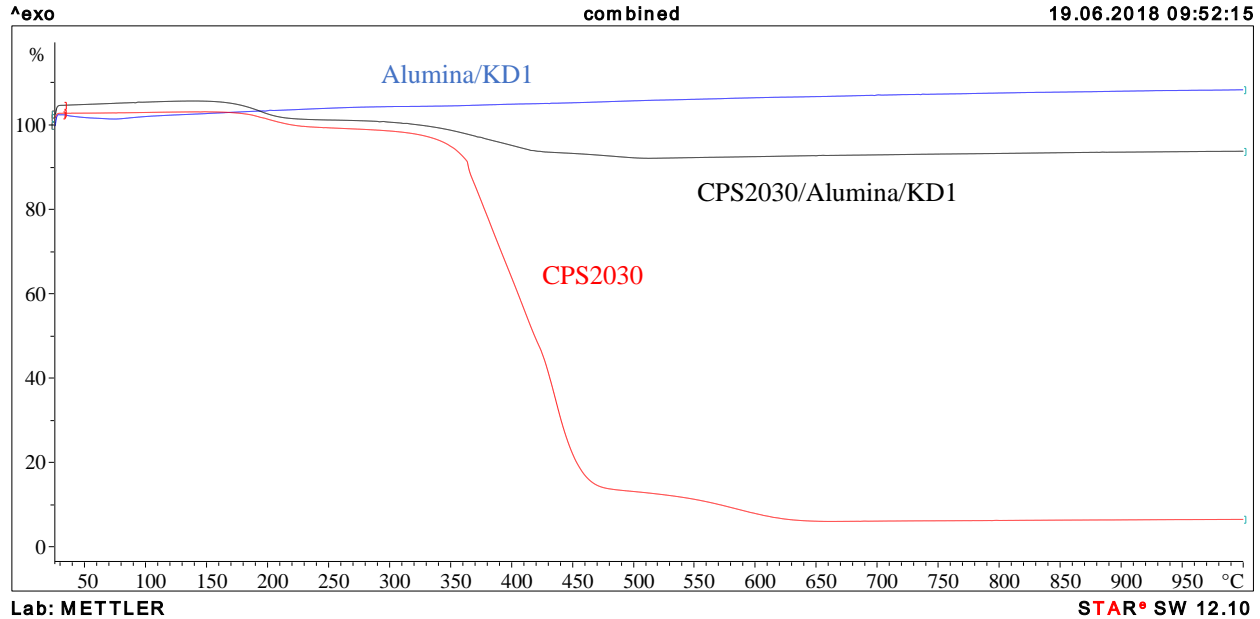
Figure 12. TGA Data in Air for Plain CPS 2030 Resin (Red line), Alumina (A15) with 1wt% KD1 (Blue line), and 55vol% A15 with 1wt% KD1 in CPS 2030 (Black Line).

4. Summary and Conclusions

Stereolithography 3D printing can be used to create high density alumina parts; however, the slurry system must be carefully chosen to allow for success. Using an initially low viscosity base resin system and a compatible dispersant is important to allow for highly loaded alumina slurries at a low viscosity. The bimodal distribution of micron sized powders (A15 SG) allowed for higher loading with less shear thickening behavior than the unimodal distribution of micron sized powders (A16 SG) due to the hydrodynamic forces present at high shear rates. A15 SG powder allowed for a maximum loading of 76%, as evaluated by the Krieger-Dougherty equation, whereas the A16 SG only allowed for a maximum loading of 61%. Parts were created on a Kudo/Digital Light Projector system with a sintered 90% theoretical density using the A15 SG powder at a 55vol% loading of alumina.

Future work will focus on increasing the A15 loading to determine the viscosity limit of the SL instrument, working towards increasing the final sintered density. Further tuning and optimization of the burnout process using the TGA results as a guide will lead to increased final density by decreasing both the inter-layer cracking and the intra-layer cracking.

5. Acknowledgements

6. Disclaimer

This paper describes objective technical results and analysis. Any subjective views or opinions that might be expressed in the paper do not necessarily represent the views of the U.S. Department of Energy or the United States Government. SAND2018-6794 C

References

Alumina, A. P. (n.d.). *Reactive Aluminas for Ceramic Applications.* SDS 387.

Halloran, J. W. (2016). Ceramic Stereolithography: Additive Manufacturing for Ceramics by Photopolymerization. *Annual Review of Materials Resaerch*, 19-28. doi:10.1146/annurev-matsci-070115-031841

Hiemenz, P. C., & Rajagopalan, R. (1997). *Principles of Colloid and Surface Chemistry.* Boca Raton: CRC Press.

Hinczewski, C., Corbel, S., & Chartier, T. (1998). Ceramic Suspensions Suitable for Stereolithography. *Journal of the European Ceramic Society*, 583-590.

Hunter, R. J. (1989). *Foundations of Colloid Science Volume II.* Great Britan: Oxford University Press.

Johansson, Emil; Lidstrom, Oscar; Johansson, Jan; Lyckfeldt, Ola; Adolfsson, Erik;. (2017). Influence of Resin Composition on the Defect Formation in Alumina Manufactured by Stereolithography. *Materials, 10*, 138. doi:10.3390/ma10020138

Li, K., & Zhao, Z. (2016). The effect of the surfactants on the formulation of UV-curable SLA alumina suspension. *Ceramics International*. doi:10.1016/j.ceramint.2016.11.143

Mettler Toledo. (n.d.). *Interpreting TGA Curves*. Retrieved from Mettler Toledo: https://www.mt.com/us/en/home/supportive_content/matchar_apps/MatChar_UC131.html

Mewis, J., & Wagner, N. J. (2012). *Colloidal Suspension Rheology.* New York: Cambridge University Press.

Schwentenwein, M., & Johannes, H. (2015). Additive Manufacturing of Dense Alumina Ceramics. *International Journal of Applied Ceramic Technology, 12*, 1-7. doi:10.1111/ijac.12319

Smith, J. P., & Messing, G. L. (1984). Sintering of Bimodally Distributed Alumina Powders. *Journal of the American Ceramic Society, 67*(4), 238-242.

Wu, H., Cheng, Y., Liu, W., He, R., Zhou, M., Wu, S., . . . Chen, Y. (2016). Effect of the particle size and the debinding process on the density of alumina ceramics fabricated by 3D printing based on stereolithography. *Ceramics International*, 17290-17294.